Space Sci Rev (2009) 147: 31–54
DOI 10.1007/s11214-009-9542-5

Interplanetary Coronal Mass Ejections Observed in the Heliosphere: 1. Review of Theory

Timothy A. Howard · S. James Tappin

Received: 6 March 2009 / Accepted: 27 May 2009 / Published online: 11 June 2009

Abstract With the recent advancements in interplanetary coronal mass ejection (ICME) imaging it is necessary to understand how heliospheric images may be interpreted, particularly at large elongation angles. Of crucial importance is how the current methods used for coronal mass ejection measurement in coronagraph images must be changed to account for the large elongations involved in the heliosphere. In this review of theory we build up a picture of ICME appearance and evolution at large elongations in terms of how it would appear to an observer near 1 AU from the Sun. We begin by revisiting the basics of Thomson scattering describing how ICMEs are detected, in this we attempt to clarify a number of common misconceptions. We then build up from a single electron to an integrated line of sight, consider the ICME as a collection of lines of sight and describe how a map of ICME appearance may be developed based on its appearance relative to each line of sight. Finally, we discuss how the topology of the ICME affects its observed geometry and kinematic properties, particularly at large elongations. This review is the first of a three-part series of papers, where a review of theory is presented here and a model is developed and used in subsequent papers.

Keywords Coronal mass ejections · Solar-terrestrial relations · Interplanetary medium

1 Introduction

Recent observations by the STEREO spacecraft, especially those by the Heliospheric Imager instruments (e.g., Harrison et al. 2008; Sheeley et al. 2008; Webb et al. 2009) have inspired a new wave of interest in the dynamics of the interplanetary medium within the space physics community. Of particular interest is the study of interplanetary coronal mass ejections (ICMEs), which are the heliospheric counterpart of coronal mass ejections (CMEs)

T.A. Howard (✉) · S.J. Tappin
Air Force Research Laboratory, National Solar Observatory, Sunspot, NM 88349, USA
e-mail: thoward@nso.edu

T.A. Howard
Department of Space Studies, Southwest Research Institute, Boulder, CO 80302, USA

(Zhao 1992; Dryer 1994). CMEs are thought to be responsible for the removal of magnetic helicity and large quantities of mass from the solar corona and may be described as clouds of plasma which originate from the Sun. They can span several tens of degrees of heliospheric latitude and have masses typically of the order of $\sim 10^{12}$–10^{13} kg. CMEs are usually observed using white light coronagraphs and generally appear as a bright loop moving away from the Sun. Farther from the Sun, ICMEs observed in white light often resemble only part of a loop, and unlike CMEs, rarely is the white light ICME structure observed to connect with the Sun. Along with CMEs, other large-scale disturbances are also observed in the corona and heliosphere, such as narrow jets and slow-moving corotating interaction regions. It is generally accepted that ICMEs are responsible for the majority of severe geomagnetic storms observed at Earth (e.g., Burlaga et al. 1981; Gosling 1993; Schwenn et al. 2005 and references therein) and thus understanding the propagation of ICMEs is vital to the forecasting of such events.

The study of heliospheric images beyond elongation angles of 20° is not new. The Solar Mass Ejection Imager (SMEI, Eyles et al. 2003; Jackson et al. 2004) has been observing since February 2003, has identified and tracked over 300 ICMEs during its 6 year lifetime (e.g., Tappin et al. 2004; Howard et al. 2006; Webb et al. 2006) and continues to do so at the time of writing. Prior to this, the zodiacal light experiments aboard the twin Helios spacecraft (Leinert et al. 1975) provided observations of ICMEs in the late 1970s and early 1980s (e.g., Jackson and Leinert 1985; Jackson and Froehling 1995). Also during both missions and throughout the 20 year gap in between, radio interplanetary scintillation observations provided and continue to provide ICME images (e.g., Hewish et al. 1985; Manoharan et al. 2001; Jones et al. 2007). While the success of the Large Angle Spectroscopic Coronagraph (LASCO, Brueckner et al. 1995) at CME detection has dramatically increased the popularity and ease of CME study in more recent years, the observational histories of CMEs and ICMEs are parallel. It may be argued that the first ICME was observed by Hewish et al. (1964) well before the first CMEs were recognised by DeMastus et al. (1973) and Tousey (1973). Certainly by 1973 several articles had appeared regarding observations of interplanetary disturbances in the heliosphere (Hewish and Symonds 1969; Houminer 1971, 1973; Houminer and Hewish 1972).

Likewise, the attempted reconstruction of 3-D ICMEs is not new. IPS observations were compared with simple 3-D phenomenological models (Tappin 1987) and with MHD simulations (Tappin et al. 1990). More recently, tomographic reconstructions by Jackson and Hick (2000), for example, fit photometric observations from the Helios spacecraft to a kinematic heliospheric model, incorporating solar rotations and solar wind flow. They have used this technique to reconstruct the 3-D structure of several ICMEs, including the usage of SMEI data on the so-called "Halloween" event in October 2003 (Jackson et al. 2006). This technique, and the theory behind it, is described in further detail in Jackson and Hick (2005).

The basic physics of the Thomson-scattering process by which coronagraphs and heliospheric imagers are able to observe CME/ICMEs has been described in detail by Billings (1966), whose analysis is derived from several texts (principally Minnaert 1930; van de Hulst 1950). Unfortunately a number of notational problems in Billings (1966) have resulted in some misunderstandings and for this reason we return to the formalism of Minnaert (1930) for the discussion in Sects. 2.1 and 3.

Most studies of CMEs have made use of a number of assumptions to simplify the geometry of the problem. For ICMEs we find that the same set of assumptions do not apply, so it is necessary to use a more complete analysis. Vourlidas and Howard (2006) have made the first steps in this direction to prepare for the observations of the Heliospheric Imagers on STEREO, but do not consider the perspective and other effects due to the three-dimensional

nature of ICMEs. Therefore in this review we attempt to clarify these issues and lay the groundwork for a fully three-dimensional treatment of the interpretation of ICME observations from heliospheric imagers. We also lay the groundwork for the development of a model which combines the theory with the geometry in order to reproduce an observed ICME.

The present paper presents a review of the theory associated with CME appearance, combining the physics responsible for the intensity of ICMEs with their geometry to produce a complete picture of apparent ICME structure. For the first time we construct this picture for ICMEs beyond 20°. To do this it is necessary that we consolidate previous theoretical work, particularly (but not exclusively) from Minnaert (1930), Billings (1966), Tappin (1987), and Vourlidas and Howard (2006). Unfortunately when considered separately, these works may be difficult to follow and can be regarded as misleading and confusing. Therefore in this review we bring together this work (along with that of Schuster 1879 and van de Hulst 1950) into a single place and attempt to resolve the confusion. We extend the theory of Thomson scattering into the heliosphere and regard the observed ICME in terms of line-of-sight integrals through a three-dimensional distribution of electron density rather than as a single beam. We consider how the appearance of the ICME changes, not only with Thomson scattering geometry, but also as a function of the distance from the observer and Sun. Finally, we consider how the relative geometry of the ICME changes with respect to the observer out to near, and beyond 90° elongation. This is the first of a series of three papers, where the theoretical groundwork established here is used to develop a new model for ICME inversion in Paper 2 (Tappin and Howard 2009), and the physical implications of the model are discussed in Paper 3 (Howard and Tappin 2009).

2 The Theory of Scattering in the Solar Corona

The idea that scattered photospheric light could be a major contributor to the observed solar corona predates the discovery of the electron (Schuster 1879). Schuster solved the problem of integrating the incident radiation over the visible region of the Sun and derived the variation of polarisation with scattering angle. Fifty years later Minnaert (1930) extended the analysis to include solar limb darkening and a quantitative scattering cross section.

In his classic monograph, Billings (1966) produced a more rigorous derivation of the scattered intensities and polarisations than Minnaert (1930) had done. Unfortunately, in our view, some issues of notation by Billings (1966) have resulted in some misunderstandings and we therefore find it necessary in this review to reiterate and expand his analysis with commentary. We review the derivations of Billings (1966) but use the formalism of Minnaert (1930), and show the proper interpretation of the quantities in the next section. Unlike these earlier authors we present the results using SI units as these will be more familiar to contemporary workers than the cgs units in use 40 years ago. In this section we begin with the treatment of the Thomson scattering on a single electron, then we place this electron in the solar corona and finally consider the effects as the electron moves further away from the Sun. It is found that the effects are different as the Sun becomes a point source, and some of the assumptions we can apply when close to the Sun break down.

2.1 Thomson Scattering

The basic scattering process for white light in the solar corona and the solar wind is that of Thomson scattering (e.g., Jackson 1975), which is a special case of the general theory of the scattering of electromagnetic waves by charged particles. The Thomson theory can be used provided two conditions are met:

1. The coherence length of the radiation is small compared with the separation of the particles, which in the case of incoherent sources means that the wavelength must be small compared with the separation. If this is not met (as is typically the case for radio waves) then the theory of coherent scattering must be used;
2. The energy of the photons is negligible compared with the rest mass energy of the scattering particles. If this is not met (e.g. for x-rays) then the theory of Compton scattering must be used.

For optical wavelengths and the densities encountered in the corona and solar wind, both of these conditions are comfortably met so we can safely use the Thomson theory throughout.

A rigorous derivation of the scattering of an electromagnetic wave by an electron is presented by Jackson (1975) and other textbooks on electrodynamics, so in this review we present a more pictorial version that allows the important features of the scattering to be visualised in preparation for the application of the theory to the Sun and the corona.

Let us consider an unpolarised monochromatic plane wave incident on an electron, as in Fig. 1(a). The electric field in the wave will cause an acceleration of the electron. The electron will then re-radiate in a pattern symmetrical about the direction of the incident wave. Since the electric field of an electromagnetic wave is always perpendicular to the direction

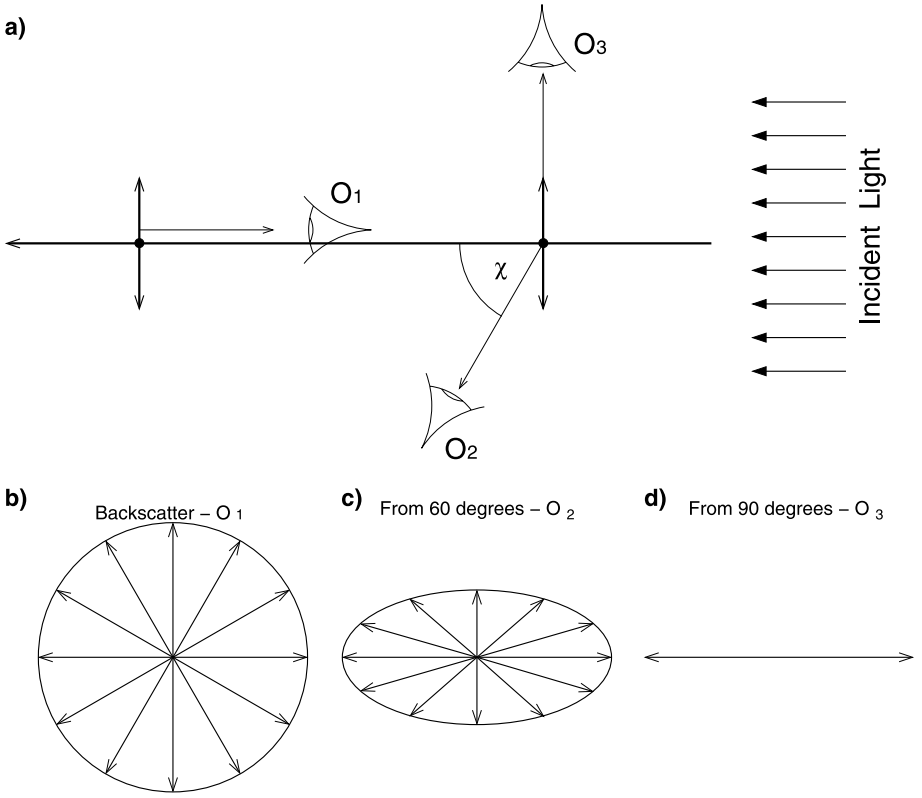

Fig. 1 Schematic demonstrating how the angular variation in Thomson scattering arises (**a**) the conceptual set up, the scattering angle χ is included for the oblique observer (O_2), (**b**)–(**d**) the scattered electric vectors as seen by observers at O_1 at $\chi = 180°$, O_2 at $\chi = 60°$ and O_3 at $\chi = 90°$ respectively

of propagation, the acceleration of the electron will be confined to the plane perpendicular to the propagation direction. Hence to an observer at a scattering angle (χ) of 0° or 180°, the electron will appear to be displaced equally in all directions and therefore the scattered light will be unpolarised (Fig. 1(b)). However, an observer at $\chi = 90°$ (Fig. 1(d)) will not see the movement of the electron along the line of sight, and so will see only a linear motion perpendicular to the direction of the incident beam, Thus that observer will see linearly polarised scattered light, but the maximum magnitude of the electric field will be the same. For an observer at an intermediate angle (Fig. 1(c)) the motion and hence the electric field in the plane of both the observer and the incident direction will be foreshortened. In this case the scattered light will be partially polarised. Hence we can see that the intensity of the component seen as transverse to the incident beam is isotropic, while the intensity of the component seen as parallel to the projected direction of the incident beam varies as $\cos^2 \chi$.

When the full electromagnetic theory is applied, we arrive at the following expression for the differential cross section (Jackson 1975):

$$\frac{\mathrm{d}\sigma}{\mathrm{d}\omega} = \frac{1}{2}\left(\frac{e^2}{4\pi\varepsilon_0 m_e c^2}\right)^2 (1 + \cos^2\chi), \tag{1}$$

where $\mathrm{d}\omega$ is an element of solid angle at the scattering angle χ, and the other symbols have their usual meanings. By integrating over all solid angles we can then derive the total cross section σ_T as

$$\sigma_\mathrm{T} = \frac{8\pi}{3}\left(\frac{e^2}{4\pi\varepsilon_0 m_e c^2}\right)^2 = \frac{8\pi}{3} r_e^2 = 6.65 \times 10^{-29}\ \mathrm{m}^2, \tag{2}$$

where r_e is the classical electron radius. A useful alternative value is the differential cross section for perpendicular scattering, which we hereafter refer to as σ_e:

$$\sigma_e = \frac{e^4}{(4\pi\varepsilon_0)^2 m_e^2 c^4} = r_e^2 = 7.95 \times 10^{-30}\ \mathrm{m}^2\,\mathrm{sr}^{-1}. \tag{3}$$

This is the Thomson cross section used by Billings (1966) which is a useful parameter for determining Thomson scattering. Billings (1966) quotes it as having units of sr^{-1} rather than the correct $\mathrm{cm}^2\,\mathrm{sr}^{-1}$ (or $\mathrm{m}^2\,\mathrm{sr}^{-1}$). This is probably the major cause of the confusion surrounding his derivations.

2.2 Application to the Solar Corona

The preceding analysis applies only to the scattering of light from a point source by a single electron or small packet of electrons. Since the solar photosphere is not a point source, it is necessary to integrate the scattering over light from the visible disk of the Sun and then to integrate along the line of sight. In this section we cover the first of these integrations, and the line-of-sight integral is considered in Sect. 3.

The integration over the solar disk was first attempted by Schuster (1879). Minnaert (1930) made the analysis quantitative, by including the fact that the scatterers are electrons (unknown in Schuster's time) and also added limb-darkening. They showed how the tangential and radial electric vector components of Thomson-scattered radiation from a single electron in the solar corona may be calculated in terms of a small number of measurable parameters.

The most conceptually difficult aspect of the integration over the visible photosphere is expressing the polarisation components from an element of the photosphere in terms of a

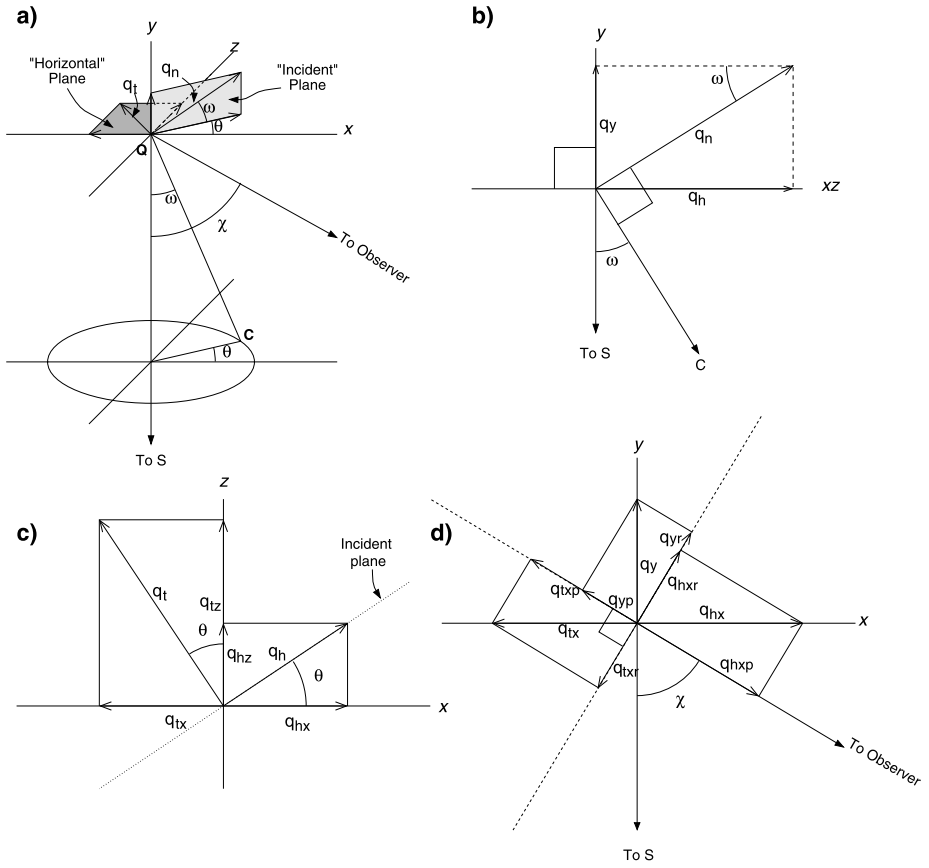

Fig. 2 The geometry involved in converting the polarisation components from an element of the photosphere to a common coordinate system. (**a**) a general overview, adapted from Fig. 6.1 of Billings (1966), (**b**) the "incident" plane, (**c**) the xy or "horizontal" plane, and (**d**) the xy or "emergent" plane

common coordinate system. For reasons which will become apparent, the chosen system is to resolve into components parallel and perpendicular to the projected radius vector joining the centre of the Sun with the scattering point. Of the available sources, only Billings (1966) handles this part explicitly, although even his treatment could be regarded, in our opinion, as overly condensed. In this review we therefore follow Billings' treatment, but emphasise the points that we have found difficult, and which he did not explain in detail. We also make some changes of notation to reduce conflicts with later parts of this review.

Let us consider the situation illustrated in Fig. 2(a) (adapted from the left-hand panel of Fig. 6.1 in Billings 1966). The coordinate system is defined such that the y-axis represents a radius vector from the centre of the Sun (S) through the scattering point Q. The x-axis is then defined such that the observer is in the xy-plane, and the z-axis is defined to complete an orthogonal set. The observer is located such that the line of sight from the observer through Q makes an angle χ with the radius vector SQ. Now consider a point C on the photosphere located such that the angle CQS is ω, and the plane CQS makes an angle θ with the xy-plane.

Since the light emitted from the element of the photosphere at C is unpolarised, it may be arbitrarily split into two equal perpendicular polarisation components. We follow Billings in

dividing into a component in the xz-plane and one in the plane CQS (Billings calls this the "incident" plane). These we denote as q_t, and q_n respectively, as the former is tangential to the solar surface, and the latter normal to the first. It should be noted here that q_n is elevated at an angle ω to the xz-plane.

The first step is to transform q_t and q_n into xyz coordinates. As we resolve the components step-by-step, it is important to realise that while we are working with intensities or powers, the decomposition is properly done with the electric vectors of the waves. Thus a component q resolved over an angle θ splits into components $q\sin^2\theta$ and $q\cos^2\theta$.

Let us firstly look at the "incident" plane (Fig. 2(b)), in which only q_n appears. Here, q_n is at an angle ω to the xz-plane, thus it resolves to one component along the y-axis and one in the xz-plane as

$$\begin{aligned} q_y &= q_n \sin^2\omega, \\ q_h &= q_n \cos^2\omega. \end{aligned} \tag{4}$$

Next we turn to the xz-plane (Fig. 2(c)), the "horizontal" plane in Billings (1966), to transform q_t and q_h into their x and z components. Since the "incident" plane is at an angle θ to the x-axis, it follows that q_h makes an angle θ with the x-axis, while q_t is at θ to the z-axis. Hence q_h is resolved into

$$\begin{aligned} q_{hx} &= q_h \cos^2\theta = q_n \cos^2\omega \cos^2\theta, \\ q_{hz} &= q_h \sin^2\theta = q_n \cos^2\omega \sin^2\theta. \end{aligned} \tag{5}$$

Similarly q_t is divided into

$$\begin{aligned} q_{tx} &= q_t \sin^2\theta, \\ q_{tz} &= q_t \cos^2\theta. \end{aligned} \tag{6}$$

The next stage of the decomposition is to transform the x and y components into the observer's coordinates in the xy or "emergent" plane (Fig. 2(d)). Here each of the x and y-directed components are resolved into a term perpendicular to the observer's line of sight and one parallel to it. We label these components with r for "radial" (since they are parallel to the solar radius vector) and p for "parallel".

The y-directed component q_y is resolved to

$$\begin{aligned} q_{yr} &= q_y \sin^2\chi = q_n \sin^2\omega \sin^2\chi, \\ q_{yp} &= q_y \cos^2\chi = q_n \sin^2\omega \cos^2\chi. \end{aligned} \tag{7}$$

The two x-directed components are similar to each other:

$$\begin{aligned} q_{hxr} &= q_{hx} \cos^2\chi = q_n \cos^2\omega \cos^2\theta \cos^2\chi, \\ q_{hxp} &= q_{hx} \sin^2\chi = q_n \cos^2\omega \cos^2\theta \sin^2\chi, \end{aligned} \tag{8}$$

and

$$\begin{aligned} q_{txr} &= q_{tx} \cos^2\chi = q_t \sin^2\theta \cos^2\chi, \\ q_{txp} &= q_{tx} \sin^2\chi = q_t \sin^2\theta \sin^2\chi. \end{aligned} \tag{9}$$

Finally we gather together the terms transverse to the radius vector and those parallel to it. At this stage we recall that q_t and q_n are equal in magnitude, so we reduce these to simply q hereafter. The transverse terms are those with electric vectors on the z axis, namely q_{hz} and q_{tz}. Thus the total transverse component q_T becomes

$$q_T = q_{hz} + q_{tz} = q(\cos^2\theta + \cos^2\omega \sin^2\theta). \tag{10}$$

The radial terms are those in the "emergent" plane and perpendicular to the observer's line of sight, namely q_{yr}, q_{hxr} and q_{txr}, so the total radial component q_R becomes

$$q_R = q_{yr} + q_{hxr} + q_{txr} = q(\sin^2\omega \sin^2\chi + \cos^2\omega \sin^2\theta \cos^2\chi + \cos^2\theta \cos^2\chi). \tag{11}$$

The intensity received at Q from the element of photosphere around the point C is given by

$$q = I \sin\theta \mathrm{d}\theta \mathrm{d}\omega = -I \mathrm{d}\theta \mathrm{d}(\cos\omega), \tag{12}$$

where I is the emitted intensity from the photosphere (in units of power per unit area per unit solid angle). Note that to be strictly correct we ought to write I as $I(\omega, \Omega)$ to allow for the limb-darkening.

To calculate the total scattered radiation, we integrate (10) and (11) over the visible portion of the photosphere, using the geometry shown in Fig. 3. This yields the two expressions:

$$I_T = \frac{\sigma_e}{2z^2} \int_{\cos\Omega}^{1} \int_{0}^{2\pi} I(\cos^2\theta + \cos^2\omega \sin^2\theta) \mathrm{d}\theta \mathrm{d}(\cos\omega), \tag{13}$$

and

$$I_R = \frac{\sigma_e}{2z^2} \int_{\cos\Omega}^{1} \int_{0}^{2\pi} I(\sin^2\omega \sin^2\chi + \cos^2\omega \sin^2\theta \cos^2\chi + \cos^2\theta \cos^2\chi) \mathrm{d}\theta \mathrm{d}(\cos\omega), \tag{14}$$

where z is the distance from Q to the observer (this is **not** the same z as in Fig. 2 and our coordinate deconstruction). Note that here we differ from Billings (1966) in two respects. Firstly we are considering just one electron (hence there is no N_e in our expressions) and

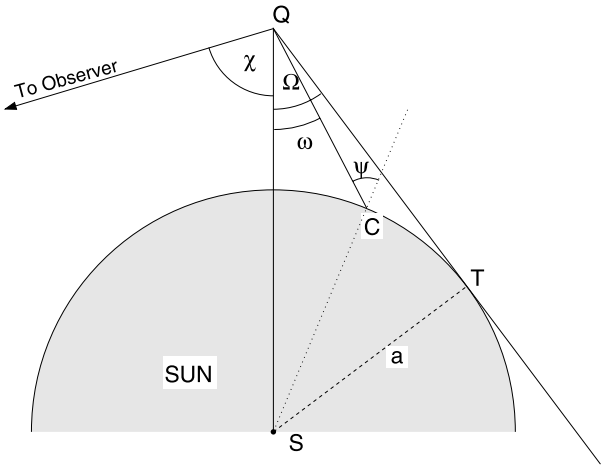

Fig. 3 The Sun and a nearby scattering point Q (modified from Fig. 6.2 of Billings 1966). The *shaded grey circle* represents the Sun with its centre at S and radius a, T is the point where the scattered point vector crosses the Sun at a tangent and Ω is the angle between the tangent from Q and the SQ vector. The line of sight (To Observer) has been added and the angle between it and the SQ vector is shown as χ. The geometry of a ray from a point C is also shown, including the angles ψ and ω

secondly since we wish to avoid the use of power per unit solid angle, we include the distance (z) to the observer as Minnaert (1930) did.

The integration over θ is relatively straightforward and yields (after eliminating the $\cos^2\chi$ and $\sin^2\omega$ terms via the trigonometric identity $\sin^2\alpha + \cos^2\alpha \equiv 1$):

$$I_T = \frac{\pi\sigma_e}{2z^2}\int_{\cos\Omega}^{1} I(1+\cos^2\omega)\mathrm{d}(\cos\omega), \tag{15}$$

and

$$I_R = \frac{\pi\sigma_e}{2z^2}\int_{\cos\Omega}^{1} I[(1+\sin^2\chi)+\cos^2\omega(1-3\sin^2\chi)]\mathrm{d}(\cos\omega). \tag{16}$$

When integrating over $\cos\omega$, it is more convenient to work in terms of $I_P = I_T - I_R$ rather than I_R as this allows the χ dependency to be factored out as

$$I_P = I_T - I_R = -\frac{\pi\sigma_e}{2z^2}\int_{\cos\Omega}^{1} I\sin^2\chi(1-3\cos^2\omega)\mathrm{d}(\cos\omega). \tag{17}$$

We now factor in the contributions of limb-darkening before we perform the second integration. Both Minnaert (1930) and Billings (1966) use an expression for the emitted intensity allowing for limb-darkening as

$$I = I_0(1-u+u\cos\psi), \tag{18}$$

and we follow their example. Here, u is the limb-darkening coefficient and is a function of wavelength, and ψ is the angle between the emitted radiation and the radius vector. To relate ψ to ω and Ω we can see from Fig. 3 that

$$\frac{\sin\psi}{\sin\omega} = \frac{|\mathbf{SQ}|}{a}, \tag{19}$$

and

$$a = |\mathbf{SQ}|\sin\Omega. \tag{20}$$

Hence we have

$$\sin\psi = \frac{\sin\omega}{\sin\Omega}. \tag{21}$$

We can now use this to convert (18) to quantities already in our integrations as

$$I = I_0\left(1-u+\frac{u(\cos^2\omega-\cos^2\Omega)^{1/2}}{\sin\Omega}\right). \tag{22}$$

So our two integrals ((15) and (17)) become

$$\begin{aligned} I_T &= I_0\frac{\pi\sigma_e}{2z^2}\left[(1-u)\int_{\cos\Omega}^{1}(1+\cos^2\omega)\mathrm{d}(\cos\omega)\right. \\ &\quad \left. + u\int_{\cos\Omega}^{1}\frac{(\cos^2\omega-\cos^2\Omega)^{1/2}}{\sin\Omega}(1+\cos^2\omega)\mathrm{d}(\cos\omega)\right] \\ &\equiv I_0\frac{\pi\sigma_e}{2z^2}\left[(1-u)C+uD\right], \end{aligned} \tag{23}$$

and

$$I_P = -I_0 \frac{\pi \sigma_e}{2z^2} \sin^2 \chi \left[(1-u) \int_{\cos \Omega}^{1} (1 - 3\cos^2 \omega) \mathrm{d}(\cos \omega) + u \int_{\cos \Omega}^{1} \frac{(\cos^2 \omega - \cos^2 \Omega)^{1/2}}{\sin \Omega} (1 - 3\cos^2 \omega) \mathrm{d}(\cos \omega) \right] \equiv I_0 \frac{\pi \sigma_e}{2z^2} \sin^2 \chi \left[(1-u)A + uB \right]. \tag{24}$$

The integrals A, B, C and D can then be evaluated to give

$$A = \cos \Omega \sin^2 \Omega, \tag{25}$$

$$B = -\frac{1}{8} \left[1 - 3\sin^2 \Omega - \frac{\cos^2 \Omega}{\sin \Omega} (1 + 3\sin^2 \Omega) \ln \left(\frac{1 + \sin \Omega}{\cos \Omega} \right) \right], \tag{26}$$

$$C = \frac{4}{3} - \cos \Omega - \frac{\cos^3 \Omega}{3}, \tag{27}$$

$$D = \frac{1}{8} \left[5 + \sin^2 \Omega - \frac{\cos^2 \Omega}{\sin \Omega} (5 - \sin^2 \Omega) \ln \left(\frac{1 + \sin \Omega}{\cos \Omega} \right) \right]. \tag{28}$$

The total intensity of the light scattered from the electrons is therefore

$$I_{tot} = (I_T + I_R) = 2I_T - I_P, \tag{29}$$

where I_0 is the intensity of the source (Sun) as a power per unit area (of the photosphere) per unit solid angle. The coefficients A, B, C and D are generally known as the van de Hulst coefficients although in fact this formulation is due to Minnaert (1930). van de Hulst (1950) made a further rearrangement of these coefficients to reduce the number of tabulated functions needed, but in the modern era of fast computers his formulation is seldom used so we do not consider it here.

Billings (1966) defines his scattered intensities I_T, I_R etc. as power per unit solid angle, while I_0 is power per unit area per unit solid angle. Thus his scattered intensities differ from those presented here (and by Minnaert 1930) by a factor of z^2. While this formalism has the convenience of removing the distance to the observer from the equations, it has the disadvantage that it is not meaningful to translate the relations into units of solar brightness[1] as the values obtained are dependent on the unit of area. In this review intensities refer to power per unit area unless explicitly stated otherwise.

Equations (25)–(29) are the primary equations used by many workers in determining the mass of a CME observed in a white light coronagraph. For example, the commonly used routine in SolarSoft is called `eltheory.pro` which is dependent on the Billings version of these equations alone, which are conveniently located on a single page (p. 150). These are valid when we are close to the Sun and its relative size is significant. In the next section we consider the effects of moving away from the Sun, where it effectively becomes a point source.

[1] As has all too often been done, most notably in the SolarSoft routine `eltheory.pro`. Fortunately for the validity of the last few decades of coronal research this error cancels out in the integrations, as shown later in this review.

2.3 Moving Away from the Sun

It may not be immediately obvious that the van de Hulst coefficients in fact bundle two related but separate effects into a single set of parameters, and their variation with distance from the source is not immediately apparent from their form. At large distances, the Sun tends towards a point source, and Ω becomes small. This has two effects, the incident radiation becomes more collimated, and it becomes fainter. Both of these are encoded in the van de Hulst coefficients. The fall-off in incident intensity is represented by coefficients tending towards $1/R^2$, while the greater collimation is seen in the decreasing difference between A and C and between B and D. Figure 4 shows the variation of the four coefficients with distance from the Sun, out to a distance of 0.1 AU (1 AU $\sim$ 215 $R_\odot$). It is perhaps surprising that well inside 0.1 AU where the Sun would still have an apparent diameter greater than 5° the deviations from the point-source case are negligible.

Vourlidas and Howard (2006) showed that the locus of all points where $\chi = 90°$ formed a sphere with the Sun-observer line as the diameter (their Fig. 1, not shown). They termed this the "Thomson surface" and showed how the scattered brightness of a single electron varied when projected radially from the Sun. They found that the distance of the electron from the Thomson surface was the dominant parameter in determining the relative brightness, and as a result made various predictions on the trajectory of ICMEs most likely to be detected by heliospheric imagers. One of their conclusions (a conclusion not supported by their results), that of limb ICMEs not being detected, is not supported by observation from the SMEI

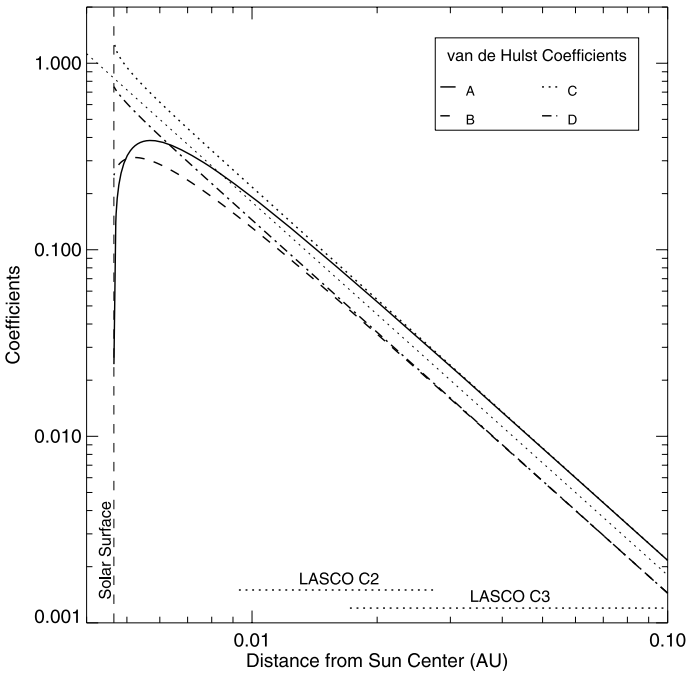

Fig. 4 The four van de Hulst coefficients, plotted as functions of R, the distance from the centre of the Sun. As the apparent size of the Sun becomes small, these coefficients tend to $1/R^2$ for distances beyond a few solar radii, as shown by comparison of the *light dotted trace* with a slope of -2. For comparison, the sky plane projection of the LASCO C2 and C3 fields-of-view are indicated

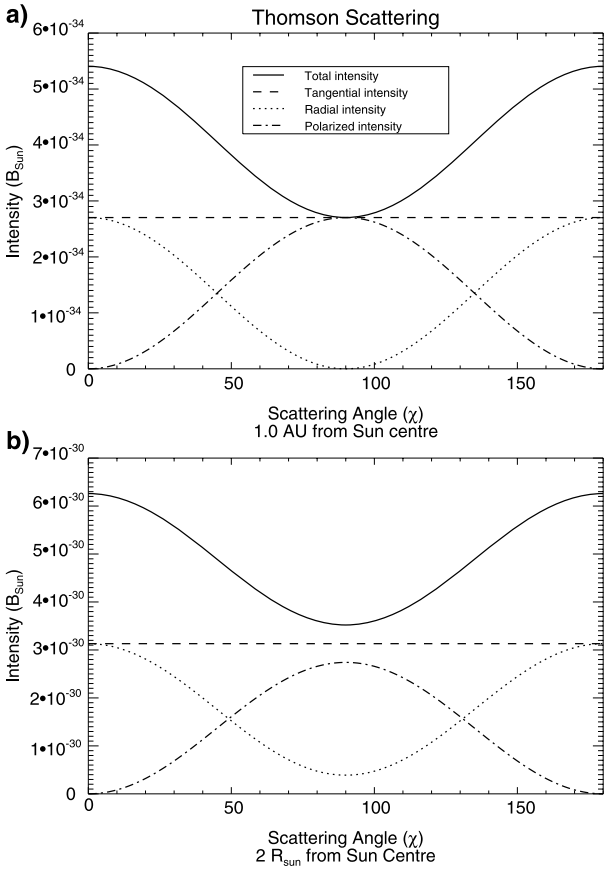

Fig. 5 Plots of total scattered intensity (power per unit solid angle) from a single electron against scattering angle χ at a distance of (**a**) 1.0 AU and (**b**) 2 $R_\odot$ from the Sun. Included are the total intensity I_{tot}, tangential and radial intensity (I_T, I_R), and the polarised intensity ($= I_T - I_R$)

instrument, which has detected limb ICMEs out to at least 0.5 AU (Howard et al. 2007). Hence we must reconsider the importance of the Thomson surface when considering the total scattered light. Of particular interest is how rapidly the scattered intensity drops off with distance from the Thomson surface.

As has already been discussed, the light received by the observer from a scattered small volume of electrons arises from a combination of two components, the tangential (I_T) and radial (I_R). I_R depends on the scattering angle χ while I_T does not ((24) and (23)). Figure 5 shows how the power per unit solid angle ($\mathcal{I}_x = z^2 I_x$ where x may be any of the components) of these components varies as a function of χ. We have shown this for a single electron at 1 AU and at 2 $R_\odot$ from the Sun. The most important point to realise is that for one electron at a fixed distance from the Sun, the scattered intensity is a *minimum* at a scattering angle of 90° (i.e. on the Thomson surface). It is also worth noting that far from the Sun the intensity of the radial component falls to near zero for perpendicular scattering, whereas near the Sun there is still a significant radial component. Physically this can be understood in terms of the apparent angular size of the Sun, for a point on the radius vector though the scattering point ($\theta = 0$ or $\omega = 0$ in Fig. 2(a)) the radial component will be zero at $\chi = 90°$, but for off-axis points there will be a radial component, and the further off-axis the greater that contribution.

The total scattered intensity seen from a location on a LOS is however governed by three separate terms:

1. The scattering efficiency as described above which is a *minimized* on the Thomson surface.
2. The incident intensity (i.e. the $1/r^2$ variation) which is *maximized* on the Thomson surface as that is where the LOS is closest to the Sun. The separate contributions of these last two terms are seldom appreciated because they are bundled together in the expressions for the scattered intensity ((23), (24) and (29)).
3. The electron density in the scattering region. This is also *maximized* on the Thomson surface, since the solar wind density falls off with distance from the Sun.

When these three terms are combined it is found that the point at which the scattered light is maximized remains that at which the LOS is orthogonal to the Sun-Q vector, i.e. on the Thomson surface. However, the result of the scattering efficiency contribution is to somewhat de-emphasise the importance of the Thomson surface, since the point on the LOS where the incident intensity and the density are greatest is also the point where the scattering efficiency is weakest. The effects of the former two are far more significant than the latter, but the partial cancelling results in a spread of observed intensity to larger distances from the Thomson surface. Furthermore, this spreading is greater at larger distances from the Sun. Hence, as we show in the next section, the distance of the observed volume from the Thomson surface is less significant when making measurements based on the assumption of Thomson scattering, but at the cost of increased uncertainty in identification of the location of the observed unit volume.

The treatment discussed in this section deals with a single electron (or small volume of electrons). CMEs, however, are large structures consisting of many electrons and are embedded in a surrounding medium consisting of the same. So, when dealing with real CMEs it is necessary to consider first a single line of sight (or rather "beam" of sight, since the CME is being observed by a detector with a particular beam size) through the CME and then a collection of lines of sight. It is also important to consider the geometry of the CME/ICME particularly at large distances from the Sun. In the following sections we build up this picture.

3 Integrated Lines of Sight

When interpreting real observations, it is crucial to note that although the scattering is presented as a line-of-sight integral this is not strictly true. It is in fact an integral though the cone of the instrument's point spread function. To illustrate this process we consider an idealised detector with a surface area δA and a beam size $\delta\omega$. The actual values of P are not important as they cancel in the final results, but understanding the process requires them.

Since the solar wind is optically thin, we do not need to consider the effects of multiple scattering.

Consider a unit volume of plasma of dimensions $(\mathrm{d}x, \mathrm{d}y, \mathrm{d}z)$, located at a distance z from the observer, as shown in Fig. 6. We define the coordinate system such that the z-axis is along the LOS and the x–y plane is the plane of the sky relative to the observer. For our detector of area δA this volume element contributes a power of

$$\mathrm{d}P = I_0 G_x(z) N_e(x, y, z)\,\mathrm{d}x\,\mathrm{d}y\,\mathrm{d}z\delta A, \tag{30}$$

where I_0 is the source intensity, N_e is the electron number density in the volume element and G_x is the scattering expression associated with I_T, I_R, I_P or I_{tot} as described in (23),

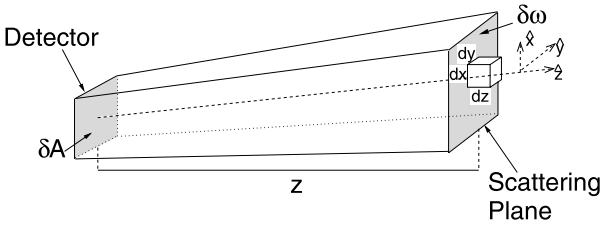

Fig. 6 Diagram demonstrating the configuration for the LOS integral calculations. A unit volume of dimensions $(\mathrm{d}x, \mathrm{d}y, \mathrm{d}z)$ is at a distance Z from the observer. The coordinate system is defined such that the z-axis is along the line of sight and the x–y plane is in the plane of the sky. The detector at the observer location has an area of δA and its field of view at Z has area $\delta\omega$

(24) and (29), hence:

$$G_T(z) = \frac{\pi\sigma_e}{2z^2}[(1-u)C + uD],$$
$$G_P(z) = \frac{\pi\sigma_e}{2z^2}[(1-u)A + uB],$$
$$G_R(z) = G_T - G_P \quad \text{and}$$
$$G_{tot}(z) = G_T + G_R = 2G_T - G_P.$$

To reduce the clutter we hereafter omit the dependencies for N_e and G unless we require them to be emphasised.

If the beam from the detector observes a solid angle of sky $\delta\omega$, then the total power received by the detector from the part of the LOS between z and $z + \mathrm{d}z$ is

$$P_{\mathrm{rec}}(z)\,\mathrm{d}z = \iint_{\delta\omega} I_0 N_e G \mathrm{d}x\,\mathrm{d}y\,\mathrm{d}z\delta A. \tag{31}$$

Since the element of solid angle $\mathrm{d}\omega$ at a distance Z observed by the detector is

$$\mathrm{d}\omega = \frac{\mathrm{d}x\,\mathrm{d}y}{z^2},$$

we may express the power received as

$$P_{\mathrm{rec}}(z)\,\mathrm{d}z = I_0 N_e z^2 G \delta A \mathrm{d}z. \tag{32}$$

It is only at this stage that we may meaningfully express the intensities in terms of the solar surface brightness by setting the power that would be received from the Sun by the observing instrument $I_0\delta A\delta\omega$ equal to 1. So when we convert (31) to units of intensity in solar brightness units it becomes

$$I_{\mathrm{rec}}(z)\,\mathrm{d}z = N_e z^2 G\,\mathrm{d}z. \tag{33}$$

Equation (33) represents the intensity contribution to a detector of a single element on the LOS. The detector, however, observes all contributions along the entire LOS. Hence, the total intensity integrated along the LOS received by the detector is

$$I_{\mathrm{rec}} = \int_0^\infty N_e z^2 G\,\mathrm{d}z. \tag{34}$$

This reduces to a simple line-of-sight integral of the expressions in Billings (1966), provided that the electron density does not vary significantly across the beam of the instrument.

The assumption typically applied when measuring CMEs is that the entire intensity is located on the Thomson surface, so the integral is reduced to simply $z_{\mathrm{T}}^2 N_e(z_{\mathrm{T}})G(z_{\mathrm{T}})$, where z_{T} is the distance from the observer to the Thomson surface. In order to test the validity of this assumption across large distances from the Sun, we consider the scattered light distributions along entire lines of sight at various elongation angles ε (elongation is the angle between the LOS and the observer-Sun vector). The geometry for a single LOS is shown in Fig. 8(a) and the distributions as functions of distance from the observer and observer-Sun-packet angle ϕ in Figs. 8(b) and (c) respectively. A similar plot to that shown in Fig. 8(b) appears in Jackson and Hick (2005) (their Fig. 3). If we had simply plotted intensity contribution in Figs. 8(b) and (c) then the difference in total scattering power would make the large-elongation traces hard to see, so we normalise by the integrated intensity such that the y-axis becomes

$$\frac{z^2 N_e(z)G(z)}{\int_0^\infty z^2 N_e(z)G(z)\mathrm{d}z}. \tag{35}$$

As shown in Fig. 8(b), the peaks in the contributions to the intensity occur on the Thomson surface as expected. However of note is the width of the peak, which becomes broader with increasing elongation. This indicates that as a volume of electrons moves away from the Thomson surface, its scattered light intensity will drop off at a less rapid rate when it is at larger distances from the Sun.

More significant for the interpretation of CME observations is the relationship of the scattered light to the observer-Sun-packet angle ϕ, as shown in Fig. 8(c). For this plot, the intensity is normalised in a similar manner, with an additional term of the rate of change of z with ϕ included. That is,

$$\frac{z^2 N_e(z)G(z)\frac{\mathrm{d}z}{\mathrm{d}\phi}}{\int_0^{\pi-\varepsilon} z^2 N_e(z)G(z)\frac{\mathrm{d}z}{\mathrm{d}\phi}\mathrm{d}\phi}, \tag{36}$$

where

$$\frac{\mathrm{d}z}{\mathrm{d}\phi} = R_0 \frac{\sin(\phi+\varepsilon)\cos\phi - \sin\phi\cos(\phi+\varepsilon)}{\sin^2(\phi+\varepsilon)}.$$

This formulation is important because CMEs are thought to expand more-or-less radially from the Sun, and so will cover a similar extent in observer-Sun-packet angle irrespective of their distance from the Sun. Here while the location of the peak varies again in accordance with the relative location of the Thomson surface, the width of the peak is almost unchanged regardless of the elongation. This shows that across a longitudinal width of around $\pm 30^\circ$ from the Thomson surface, the scattered contribution is relatively unchanged, and that this trend is largely independent of the direction of the LOS. This explains why limb CMEs may be observed beyond 0.5 AU, such as those observed by SMEI. Physically, this implies that the assumption of Thomson surface localisation when estimating CME/ICME mass is surprisingly robust even at large elongations, but the accurate determination of ICME structure becomes more uncertain.

4 Constructing the ICME

It seems clear that to overcome the difficulties associated with CME/ICME structure determination at larger elongations, it is necessary to consider the ICME as a complete structure.

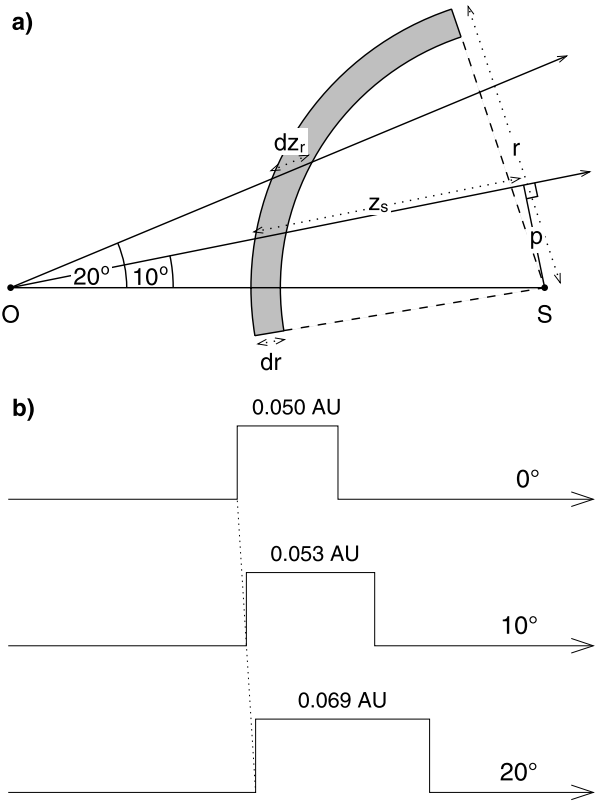

Fig. 7 Illustration of the CME function relative to different lines of sight. (**a**) A simple ICME spherical shell structure, with an angular with of ∼90°. Here, the ICME is ∼0.5 AU from the Sun and the ICME has a uniform thickness of d$r = 0.05$ AU. It also has a uniform density of 2 times the base level electron density. For generality the ICME central axis is offset from the Sun-observer line. Three lines of sight are shown by way of example, at elongations 0° (the Sun-observer line), 10° and 20°. (**b**) The ICME function for each LOS. The ICME has a value of 2 across its thickness and the LOS function has a value of 1 everywhere else. The thickness of the ICME through each LOS is determined by the angle at which the LOS passes through the ICME. In this case the ICME function is wider for the 20° elongation LOS than the 10° LOS. The Sun-observer line passes normally through the ICME, and so the ICME function on this LOS has a thickness of exactly 0.05 AU

From a mathematical point of view, a CME can be represented as a function multiplying the background solar wind. We chose to use a multiplicative rather than an additive ICME density formulation partly because it is more convenient in the simulations presented in Paper 2 of this series (Tappin and Howard 2009), and also because it appears to be a closer approximation to the evolution of a disturbance in the solar wind (e.g., Hundhausen 1973). We may thus express the resultant intensity on a LOS i as

$$I_{\mathrm{rec}_i} = \int_0^\infty N_e z^2 F_i \, G_i \, \mathrm{d}z, \tag{37}$$

where F_i refers to the CME function along the ith LOS. For example, consider the simplest form of CME structure, a spherical shell as shown in Fig. 7(a). In this case the simulated ICME has an angular width of ∼90° and a uniform thickness of 0.05 AU, and we have chosen a time at which the leading edge of the ICME is ∼0.5 AU from the Sun. We express the ICME density as a fractional change of the baseline electron density, and here assume the ICME also has a uniform density of twice the base level electron density. For generality the ICME central axis is offset from the Sun-observer line. Two lines of sight are shown at elongations 10° and 20° and their functions, along with that at elongation of 0° (the Sun-observer line), are shown in Fig. 7(b). The ICME has a value of 2 across its thickness and the LOS function has a value of 1 everywhere else. The thickness of the ICME through each LOS is determined by the angle at which the LOS passes through the ICME. In this case the ICME function has a width of 0.053 AU for the 10° elongation LOS and a width of

0.069 AU for the 20° LOS. Because this is a spherical shell the Sun-observer line passes normally through the ICME, and so the thickness of the ICME function on this LOS is exactly 0.05 AU. The ICME thickness along any LOS may be calculated from

$$\mathrm{d}z_r = [(r + \mathrm{d}r)^2 - p^2]^{1/2} - z_s, \tag{38}$$

where r is the location of the outer edge of the ICME, $\mathrm{d}r$ is the ICME thickness, p is the distance from the Sun to the Thomson surface and z_s is the distance along the LOS from the leading edge to the Thomson surface (Tappin 1987).

The observed ICME is therefore a compilation of all the LOS functions that pass through the ICME structure. The most convenient way to express this is to produce a map such that each LOS integral represents a single point. This may be produced in any projection, but for all-sky imaging it is generally convenient to use an equal-area projection such as Mollweide's or Aitoff's projections (e.g., Hinks 1912; Leighly 1955, or any textbook on map projections). This is the procedure we have adopted in the model devised in Paper 2 of this series.

4.1 Polarization

At this point it is worthwhile to pause and consider the effects of polarisation in the region observed by heliospheric imagers. Space-borne coronagraphs have had polarisation capabilities from the earliest days, but the heliospheric images to date have not, and it is useful to see if this would be a valuable capability.

The degree of polarisation is customarily defined as

$$p = \frac{I_T - I_R}{I_T + I_R} = \frac{I_P}{I_{tot}}. \tag{39}$$

If we perform the integrations of (34) for the total and polarised components, at various elongations we find that the degree of polarisation exceeds 60% to elongations around 100° (Fig. 9(a)). This means that it should certainly be possible to measure polarisations at large elongations.

Why is this relevant to ICME observation? The main reason is that the weighting along the LOS is different for the different components. We illustrate this in Fig. 9(b), which has a similar format to Fig. 8(c), but here we look at the different polarisation components for a single LOS at an elongation of 60°. This shows that any feature that lies near the Thomson surface will be seen strongly in the tangential component, but weakly in the radial component. Conversely a feature far from the Thomson surface will be relatively stronger in the radial component. Hence we may extract three-dimensional information on the location of the ICME, information that has become obscurred by the spreading across the LOS by the scattering minimum discussed in Sect. 3.

In addition, although information on the polarisation of the F-corona and the Zodiacal light is hard to find, what is available (Koutchmy and Lamy 1985; Kimura and Mann 1998) suggests that it should be less than that for the F-corona and the solar wind. This would mean that the background levels in polarised light would be lower than in unpolarised. So, relatively speaking it could be easier to observe the ICME against the background.

In the next section we consider how the structure of the ICME translates into what we observe on the sky.

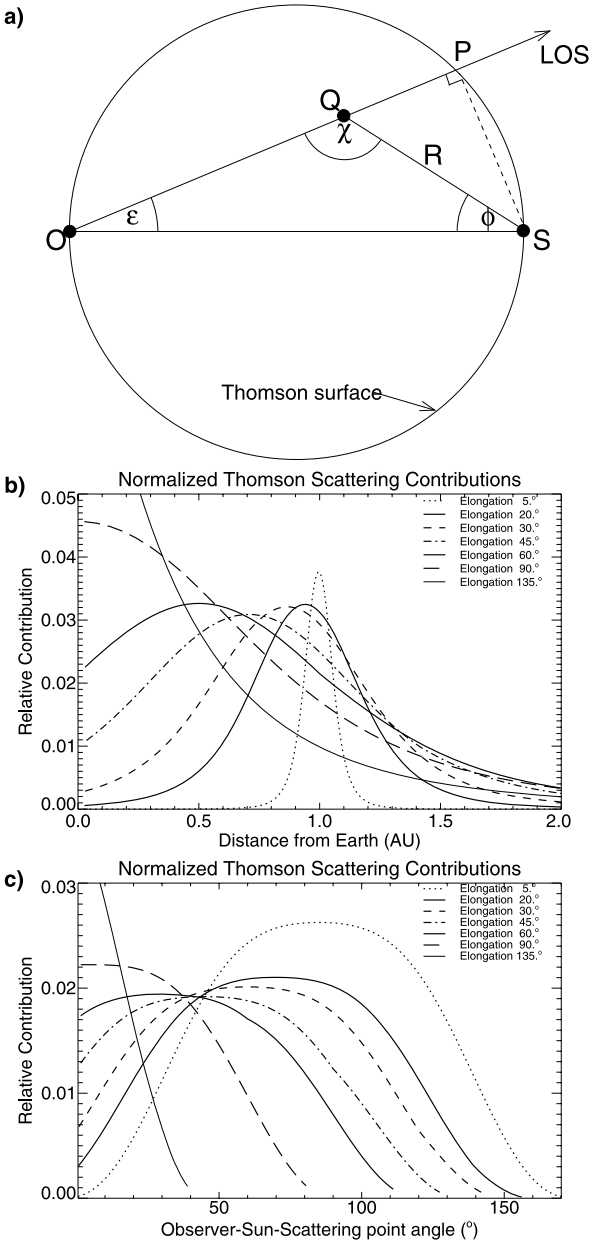

Fig. 8 (**a**) Diagram of the relevant vectors and angles to the plots below. Shown are the LOS, Sun-Q vector SQ and Sun-observer line SO. The elongation ε and Sun-observer packet angle ϕ are indicated along with the location of the Thomson surface (the LOS always meets the Thomson surface at point P). (**b**) and (**c**) Normalised scattered intensity vs. (**b**) distance from the observer in AU and (**c**) observer-Sun-packet angle relative to solar disk centre

5 The Effects of ICME Geometry

Up to this stage we have considered the effects of Thomson scattering, first on a single electron in free space, then one in the corona and the heliosphere. We have gradually built up a picture of how an ICME is imaged, by first considering a single line (or beam) of sight and then as an integration of lines of sight along with a mathematical representation for a CME/ICME. The final stage of this analysis is to consider the effects of the structure

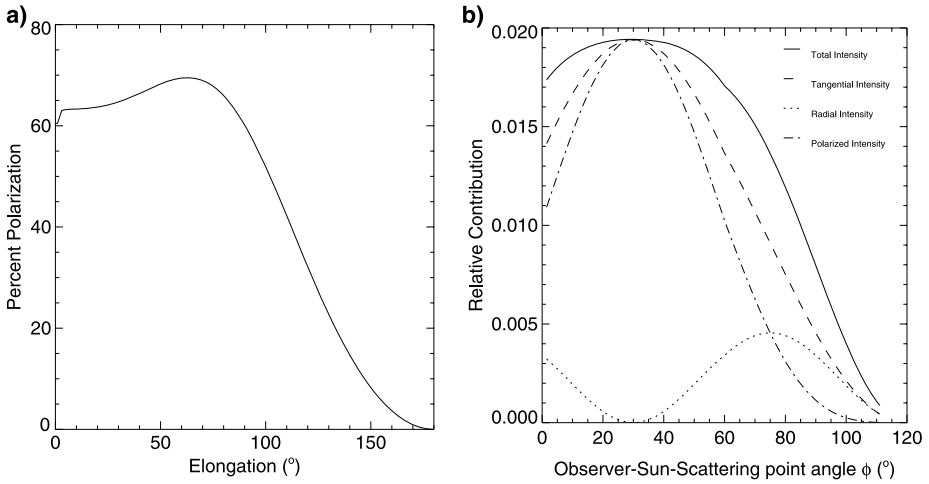

Fig. 9 The behaviour of polarisation in the heliospheric imager region of the sky. (**a**) The degree of polarisation from the quiet solar wind as a function of elongation. (**b**) The LOS weighting of the different components

of the CME/ICME relative to an observer. In this section we consider this by applying a large structure to the above analysis with particular emphasis on the apparent changes to the observed leading edge of the CME/ICME. The leading edge is the most commonly measured feature in white light images when one is calculating kinematic parameters.

In this section we intend to demonstrate the effects of the most basic of CME structures, as even in these cases the effects can become complex rather quickly. We therefore assume the CME to take the form of an expanding spherical bubble and then as an expanding spherical shell. These are commonly-used basic structures and demonstrate the effects of geometry very well. We acknowledge that in the real world the structure can be much more complex, for example may contain multiple structures or may not be geometrically symmetric about the central axis. We do believe, however, that for a demonstration of these effects, these basic structures are appropriate. We have also found that the basic structure of many ICMEs observed in white light images can be approximated by simple variations of these basic structures, such as distortion, size and direction. This is demonstrated in Papers 2 and 3 of this series (Tappin and Howard 2009; Howard and Tappin 2009).

Consider the diagrams in Fig. 10. Here we have considered two simple forms for the ICME: a spherical ICME, or expanding bubble of material moving away from the Sun (Figs. 10(a)–(c)); and a simple shell (Figs. 10(d)–(f)). These basic structures are the foundation for the ICME reconstruction in Paper 2. The Sun S and observer O are fixed points, and the central axis or diameter of the ICME is arbitrarily oriented so it has a component that is observer-directed. Figures 10(a) and (d) show the ICME at three different locations, at small, medium and large distances from the Sun. The observed leading edge of the ICME (i.e. the point where the ICME distance is measured) is the point at which the LOS is a tangent to the ICME. This point, indicated by the $\times$ symbols in Figs. 10(a) and (d), moves closer to the observer as the ICME expands. Thus, if one assumes the same point on the ICME is measured each time, indicated by the $\circ$ symbols, then the distance measurements of the ICME would appear to be larger than they actually are (the $+$ symbols). Consequently, speed measurements of ICMEs at large elongations would appear to be much larger. This has been seen in SMEI measurements beyond about 50° elongation.

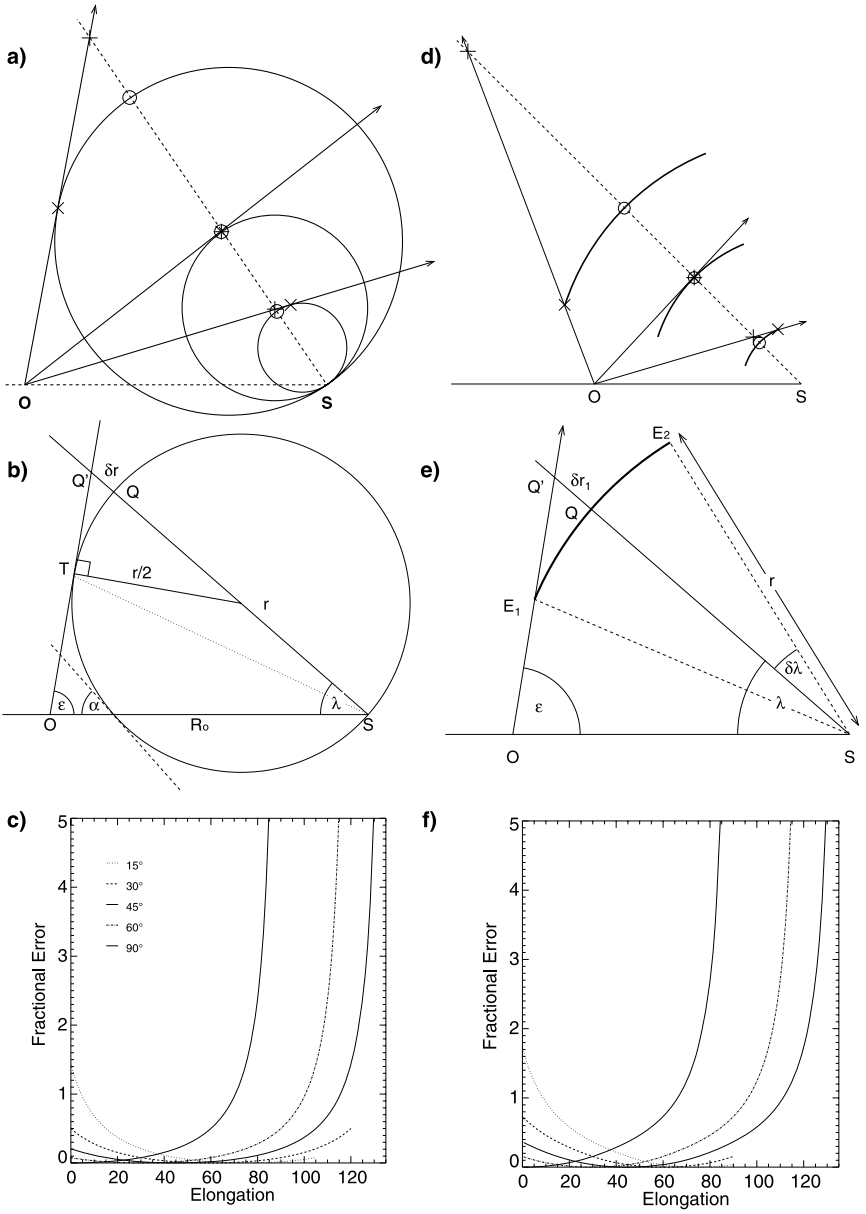

Fig. 10 Diagrams of basic ICME structures, (**a**)–(**c**) the expanding bubble and (**d**)–(**f**) a simple shell with a semi-vertical angle of 30°. (**a**) & (**d**) The ICME at three different locations during its expansion, at small, medium and large distances. The tangent drawn from the observer O across the CME surface shows the location of the relative leading edge. The $\times$ symbols represent the location of the leading edge seen by the observer the $\circ$ symbols show the true location of the leading edge at the central location and the $+$ symbols the inferred location of the leading edge based on the central location. (**b**) & (**e**) The geometry allowing the derivation of the relationship between the difference in measured distance at a given point as a function of elongation. (**c**) & (**f**) Plot of $\delta r/r$ vs. ε for $\lambda = [15, 30, 45, 60, 90]°$. For the shell (**f**) the value of $\delta\lambda$ is 30°. This shows how the difference between the actual ICME distance and measured distance varies with elongation

Let us first consider the situation illustrated in Fig. 10(a). The idealised "bubble" ICME is ejected at an angle to the Sun-observer line, and for this argument we assume that the angle has been determined from other sources. It can be seen from Fig. 10(a) that when the LOS forms a tangent with the central axis of the ICME, then our inferred size of the ICME will be correct, but at all other times we will infer a size greater than the true size of the ICME. To quantify this, consider the geometry shown in Fig. 10(b). Here the assumed measured point on the ICME is Q and the actual measured point is Q′. T represents the point on the sphere where the LOS is tangent and crosses the ICME, i.e. the observed leading edge. The distance of the assumed measured point from the Sun is r and the actual measured distance of this point is $r + \delta r$. So the difference between the measured distance and true distance is δr. From this diagram it can be shown that

$$r + \delta r = \frac{r}{2}(1 + \mathrm{cosec}(\lambda + \varepsilon)), \tag{40}$$

or

$$r = \frac{2R_0 \sin\varepsilon \ \mathrm{cosec}(\lambda + \varepsilon)}{1 + \mathrm{cosec}(\lambda + \varepsilon)}, \tag{41}$$

where R_0 is the distance from the observer to the Sun (typically 1 AU). Also shown in Fig. 10(b) is the angle α which is the angle the tangent to the CME along the Sun-observer line makes to the Sun-observer line. When $\alpha + \varepsilon = 180°$ the leading edge of the ICME has reached the observer, so beyond this point calculations of δr are meaningless. This represents the limit of the calculations. It can readily be shown that $\lambda + \alpha \equiv 90°$.

Figure 10(c) shows the variation of $\delta r/r$ with ε for the ICME with its central axis at $\lambda = [15, 30, 45, 60, 90]°$.

This shows that for elongations such that $\varepsilon + \lambda$ is close to 90°, the error in distance is relatively small, but as $\varepsilon + \lambda$ approaches 0° or 180° the inferred size diverges. When $\varepsilon + \lambda$ is 124° the error is about 10%, and by the time $\varepsilon + \lambda$ is 150° the error is 50%, and then rises rapidly to a factor of 2 near 160°.

The case of the simple shell shown in Figs. 10(d) and (e) is a little more complicated as there are three situations to consider:

$$\begin{aligned}
&r = R_0 \sin\varepsilon \quad \text{when the LOS is a tangent to the front,} \\
&\quad \text{i.e. } 90° - (\lambda + \delta\lambda) < \varepsilon < 90° - (\lambda - \delta\lambda); \\
&r = R_0 \sin\varepsilon \ \mathrm{cosec}(\varepsilon + (\lambda - \delta\lambda)) \quad \text{when the LOS contacts at } \mathrm{E}_1, \\
&\quad \text{i.e. } \varepsilon > 90° - (\lambda - \delta\lambda); \\
&r = R_0 \sin\varepsilon \ \mathrm{cosec}(\varepsilon + (\lambda + \delta\lambda)) \quad \text{when the LOS contacts at } \mathrm{E}_2, \\
&\quad \text{i.e. } \varepsilon < 90° - (\lambda + \delta\lambda).
\end{aligned} \tag{42}$$

Here $\delta\lambda$ is the semi-vertical angle of the cone swept out by the shell. The value of $r + \delta r$ remains as in (40). Figure 10(f) shows $\delta r/r$ for the case of a simple shell of semi-vertical angle 30° at the same values of λ as for the bubble. While the detailed values are different, the qualitative effect of overestimating the leading-edge distance at both large and small elongations remains the same as for the bubble.

The examples discussed above are for the very simple cases of an ICME as a uniform, expanding spherical bubble and a spherical shell. Even here it is clear that the relative location of the central axis of the ICME to that of the Sun-observer line and the angular extent

of the ICME are crucial in correcting for ICME geometry in distance measurements. CMEs and ICMEs, however, do not correspond exactly to these simple forms, nor are they even symmetric about their central axis. Thus it is clear that many assumptions are required to approximately measure ICMEs at large elongations even to a first order level.

We have found that many of the problems associated with the application of these simple structures can be reduced by careful consideration of the physics responsible for ICME appearance in white light. For example, careful treatment of individual structures separately overcomes the issue of multiple structures and leading edge measurements overcome the sometimes fuzziness of many ICME images. The application of this analysis to the modelling of ICME observations by heliospheric imagers is discussed in Paper 2 (Tappin and Howard 2009), along with a consideration of the advantages and disadvantages. The physical implications of such a technique are explored further in Paper 3 (Howard and Tappin 2009).

6 Summary

The physics that determine the appearance of CMEs dates from well before the discovery of the CME, and even before the discovery of the electron. We have shown the complexities of the theory in this review and have clarified some of the misconceptions and mathematical procedures used in the commonly referenced texts. We have also for the first time expanded the theory to include the structure of the CME at large distances from the Sun. It is our intention for this review to be used as a contemporary theoretical tool for those studying CMEs and ICMEs, and to replace the sometimes confusing text of Billings (1966). It is also our intention to establish the theoretical framework on which the model produced in Paper 2 was built.

From the analyses and discussions presented in this review, it is very clear that many of the assumptions generally used in the analysis of CME observations must be treated with caution, especially at larger distances from the Sun.

1. As has already been noted by Vourlidas and Howard (2006) the assumption that the scattering lies in the plane of the sky is not valid at large elongations, rather the scattering is peaked on the so-called Thomson surface, a 0.5 AU radius (when observing from Earth) sphere of which the Sun-observer line is a diameter.

   It is however important to realize that this represents the peak of the scattering only because the density and incident illumination maximize here. The specific scattering is in fact a minimum on the Thomson surface.
2. In distance the scattering becomes more spread out along the LOS as the elongation becomes larger. However when viewed in terms of the angle from the scattering point to the intersection of the LOS and the Thomson surface as seen from the Sun, the width of the scattering is almost independent of the elongation. This width is large with little variation within 30°–40° of the Thomson surface.

   A direct result of this is that the computation of CME/ICME mass made on the assumption that the entire mass excess lies on the Thomson surface is quite accurate for CMEs within 30°–40° of the Thomson surface. However this comparative insensitivity to direction means that positional observations or calculations must be used to accurately determine the direction. Imagers observing polarised light may assist in resolving this issue.

3. We have however also shown that the interpretation of observations of the leading edge of ICMEs is fraught with difficulties especially at large elongations, where the simple assumptions that one is always looking at the same part of the ICME can lead to very large errors in the estimated height of the leading edge.

While these considerations apply for all CME/ICME observations, their importance becomes far greater for ICMEs at a substantial fraction of 1 AU from the Sun, as are currently being observed both by SMEI and by the HI-2 imagers on STEREO.

The examples we have presented here are extremely simplified, and in this simple form cannot be considered adequate to model real disturbances. For this reason we present a system of models that can generate a hypercube of synthetic ICME sky maps with a range of geometries and directions in Paper 2 of this series (Tappin and Howard 2009). These can be matched with observations of ICMEs and an estimate thus made of at least the gross properties of the real structures. The model is developed based on SMEI observations and applied to two events with remarkably accurate results. In Paper 3 of this series (Howard and Tappin 2009) the model is modified to accommodate for the STEREO HI data and applied to a single Earth-directed ICME observed by several imaging and in-situ instruments, including SMEI and both STEREO spacecraft.

Acknowledgements This work is supported in part by the National Research Council Fellowship Program, funded by AFOSR contract F49620-02C-0015. The National Solar Observatory is operated by AURA, Inc., under cooperative agreement with the National Science Foundation. Partial support for NSO is provided by the USAF under a Memorandum of Agreement.

References

D.E. Billings, *A Guide to the Solar Corona* (Academic Press, San Diego, 1966)
G.E. Brueckner, R.A. Howard, M.J. Koomen, C.M. Korendyke, D.J. Michels, J.D. Moses, D.G. Socker, K.P. Dere, P.L. Lamy, A. Llebaria, M.V. Bout, R. Schwenn, G.M. Simnett, D.K. Bedford, C.J. Eyles, Sol. Phys. **162**, 357 (1995)
L.F. Burlaga, E. Sittler, F. Mariani, R. Schwenn, J. Geophys. Res. **86**, 6673 (1981)
H.L. DeMastus, W.J. Wagner, R.D. Robinson, Sol. Phys. **100**, 449 (1973)
M. Dryer, Space Sci. Rev. **67**, 363 (1994)
C.J. Eyles, G.M. Simnett, M.P. Cooke, B.V. Jackson, A. Buffington, N.R. Waltham, J.M. King, P.A. Anderson, P.E. Holladay, Sol. Phys. **217**, 319 (2003)
J.T. Gosling, J. Geophys. Res. **98**, 18937 (1993)
R.A. Harrison, C.J. Davis, C.J. Eyles, D. Bewsher, S.R. Crothers, J.A. Davies, R.A. Howard, D.J. Moses, D.G. Socker, J.S. Newmark, J.-P. Halain, J.-M. Defise, E. Mazy, P. Rochus, D.F. Webb, G.M. Simnett, Sol. Phys. **247**, 171 (2008)
A. Hewish, M.D. Symonds, Planet. Space Sci. **17**, 318 (1969)
A. Hewish, P.F. Scott, D. Wills, Nature **203**, 1214 (1964)
A. Hewish, S.J. Tappin, G.R. Gapper, Nature **314**, 137 (1985)
A.R. Hinks, *Map Projections* (Cambridge Univ. Press, Cambridge, 1912)
T.A. Howard, S.J. Tappin, Space Sci. Rev. (2009, this issue)
T.A. Howard, D.F. Webb, S.J. Tappin, D.R. Mizuno, J.C. Johnston, J. Geophys. Res. **111**, A04105 (2006). doi:10.1029/2005JA011349
T.A. Howard, C.D. Fry, J.C. Johnston, D.F. Webb, Astrophys. J. **667**, 610 (2007)
Z. Houminer, Nat. Phys. Sci. **231**, 165 (1971)
Z. Houminer, Planet. Space Sci. **21**, 1617 (1973)
Z. Houminer, A. Hewish, Planet. Space Sci. **20**, 1703 (1972)
A.J. Hundhausen, J. Geophys. Res. **78**, 1528 (1973)
B.V. Jackson, H.R. Froehling, Astron. Astrophys. **299**, 885 (1995)
B.V. Jackson, P. Hick, Adv. Space Res. **25**, 1875 (2000)
B.V. Jackson, P. Hick, in *Solar and Space Weather Radiophysics, Current Status and Future Developments*, ed. by D.E. Gary, C.U. Keller, vol. 314 (Kluwer Academic, Dordrecht, 2005), p. 355, Chap. 17

B.V. Jackson, C. Leinert, J. Geophys. Res. **90**, 10759 (1985)
B.V. Jackson, A. Buffington, P.P. Hick, R.C. Altrock, S. Figueroa, P.E. Holladay, J.C. Johnston, S.W. Kahler, J.B. Mozer, S. Price, R.R. Radick, R. Sagalyn, D. Sinclair, G.M. Simnett, C.J. Eyles, M.P. Cooke, S.J. Tappin, T. Kuchar, D.R. Mizuno, D.F. Webb, P.A. Anderson, S.L. Keil, R.E. Gold, N.R. Waltham, Sol. Phys. **225**, 177 (2004)
B.V. Jackson, A. Buffington, P.P. Hick, D.F. Webb, J. Geophys. Res. **111**, A04S91 (2006). doi:10/1029/2004JA010942
J.D. Jackson, *Classical Electrodynamics*, 2nd edn. (Wiley, New York, 1975)
R.A. Jones, A.R. Breen, R.A. Fallows, A. Canals, M.M. Bisi, G. Lawrence, J. Geophys. Res. **112**, A08107 (2007). doi:10.1029/2006JA011875
H. Kimura, I. Mann, Earth Planets Space **50**, 493 (1998)
S. Koutchmy, P.L. Lamy, in *Properties and Interactions of Interplanetary Dust*, ed. by R.H. Giese, P. Lamy (Springer, Berlin, 1985), p. 63
J.B. Leighly, Geogr. Rev. **45**, 246 (1955)
C. Leinert, H. Link, E. Pitz, N. Salm, D. Knuppleberg, Raumfahartforschung **19**, 264 (1975)
P.K. Manoharan, M. Tokumaru, M. Pick, P. Subramanian, F.M. Ipavich, K. Schenk, M.L. Kaiser, R.P. Lepping, A. Vourlidas, Astrophys. J. **559**, 1180 (2001)
M. Minnaert, Z. Astrophys. **1**, 209 (1930)
A. Schuster, Mon. Not. R. Astron. Soc. **40**, 35 (1879)
R. Schwenn, A. Dal Lago, E. Huttunen, W.D. Gonzalez, Ann. Geophys. **23**, 1033 (2005)
N.R. Sheeley Jr., A.D. Herbst, C.A. Palatchi, Y.-M. Wang, R.A. Howard, J.D. Moses, A. Vourlidas, J.S. Newmark, D.G. Socker, S.P. Plunkett, C.M. Korendyke, Astrophys. J. **675**, 853 (2008)
S.J. Tappin, Planet. Space Sci. **35**, 271 (1987)
S.J. Tappin, T.A. Howard, Space Sci. Rev. (2009, this issue)
S.J. Tappin, Z.K. Smith, M. Dryer, Planet. Space Sci. **38**, 955 (1990)
S.J. Tappin, A. Buffington, M.P. Cooke, C.J. Eyles, P.P. Hick, P.E. Holladay, B.V. Jackson, J.C. Johnston, T. Kuchar, D. Mizuno, J.B. Mozer, S. Price, R.R. Radick, G.M. Simnett, D. Sinclair, N.R. Waltham, D.F. Webb, Geophys. Res. Lett. **31**, L02802 (2004). doi:10.1029/2003GL018766
R. Tousey, Space Res. **13**, 713 (1973)
H.C. van de Hulst, Bull. Astron. Inst. Neth. **11**, 135 (1950)
A. Vourlidas, R.A. Howard, Astrophys. J. **642**, 1216 (2006)
D.F. Webb, D.R. Mizuno, A. Buffington, M.P. Cooke, C.J. Eyles, C.D. Fry, L.C. Gentile, P.P. Hick, P.E. Holladay, T.A. Howard, J.G. Hewitt, B.V. Jackson, J.C. Johnston, T.A. Kuchar, J.B. Mozer, S. Price, R.R. Radick, G.M. Simnett, S.J. Tappin, J. Geophys. Res. **111**, 12101 (2006). doi:10.1029/2006JA011655
D.F. Webb, T.A. Howard, C.D. Fry, T.A. Kuchar, D. Odstrĉil, B.V. Jackson, M.M. Bisi, R.A. Harrison, J.S. Morrill, R.A. Howard, J.C. Johnston, Sol. Phys. **256**, 239 (2009)
X.-P. Zhao, J. Geophys. Res. **97**, 15051 (1992)